TUDelft

Delft University of Technology

A two-dimensional ordinary state-based peridynamic model for surface fatigue crack propagation in railheads

Ma, Xiaochuan; Wang, Li; Xu, Jinhui; Feng, Qingsong; Liu, Linya; Chen, Huapeng

Important note
To cite this publication, please use the final published version (if applicable).
Please check the document version above.

A two-dimensional ordinary state-based peridynamic model for surface fatigue crack propagation in railheads

Xiaochuan Ma [a,*], Li Wang [b,*], Jinhui Xu [a], Qingsong Feng [a], Linya Liu [a], Huapeng Chen [a]

[a] State Key Laboratory of Performance Monitoring Protecting of Rail Transit Infrastructure, East China Jiaotong University, Nanchang 330013, China
[b] Section of Railway Engineering, Department of Engineering Structure, Faculty of Civil Engineering and Geosciences, Delft University of Technology, Delft, the Netherlands

ABSTRACT

Based on ordinary state-based peridynamic theory, a 2D peridynamic model has been established to investigate fatigue crack propagation in railheads. The proposed model is verified in terms of rail deformation under a quasi-static load and the ductile material-related fatigue failure model. Good agreements have been achieved between a finite element model and the experimental results. With the proposed model, the effects of the initial crack angle, initial crack length and wheel-rail friction coefficient on crack propagation in railheads are studied. This research provides a new method for studying crack propagation in railheads.

1. Introduction

In railway transport, wheel-rail contact occurs when the train travels on the track structure. With repetitive rolling contact, fatigue cracks develop at the railhead surface [1]. In recent years, increasing train speeds and axle loads have caused higher wheel-rail contact stress, which results in more fatigue cracks at the railhead, leading to significantly higher rail maintenance costs [2]. Moreover, if measures are not taken in time to restrain crack propagation, rail spalling and even breakage can eventually occur [3], severely threatening the operational safety of trains. Therefore, it is of great importance to study railhead fatigue crack propagation to ensure train operation safety and to reduce rail maintenance work.

Many experimental studies have been conducted to study fatigue crack propagation at railheads. Usually, two kinds of methods are used in these studies. One uses a double-disc machine, and the other uses metallographic analysis.

In the first method, samples are taken from both the wheel tread and railhead and mounted on a double-disc machine, where the two discs rotate in relation to each other to simulate wheel-rail rolling contact. The crack propagation behaviour is observed during this process. Using this method, researchers have studied how crack propagation is affected by material attributes [4], ambient temperature [5], friction [6], initial defects [7], contact stress [8], sliding rate [9], and rolling velocity [10]. For the second method, crack propagation is studied from the point of view of metallography. For example, Dhar et al. [11] took a damaged point rail made of Hadfield steel as the object of research and analysed the mechanism of crack formation from the perspectives of surface material hardening and crystal distribution characteristics. Masoumi et al. [12] studied the effects of material microstructure and

---

Nomenclature

Notation	specification
δ	Horizon
H	Neighborhood of the particle $\mathbf{x}$ within the horizon δ
$\mathbf{x}, \mathbf{x}'$	Position vectors of the particles before the object is deformed
$\mathbf{u}, \mathbf{u}'$	Displacement vectors of the particles after the object is deformed
$\boldsymbol{\xi}$	Relative position vector of particles before the object is deformed
$\boldsymbol{\eta}$	Relative displacement vector of particles after the object is deformed
ρ	Mass density of the particle
$\mathbf{b}$	External force density of the particle
$\underline{\mathbf{T}}[\mathbf{x}, t], \underline{\mathbf{T}}[\mathbf{x}', t]$	Force vector states acting on the particles respectively
$\underline{w}$	Influence function
$\underline{x}$	Reference position function
q_s	Weighted volume
θ_s	Nonlocal plane dilatation
$\underline{e}_s^d$	Plane deviatoric extension scalar state
K, G, E, ν	Bulk modulus, shear modulus, elastic modulus, Poisson's ratio
ψ	Scalar function used to represent bond broken
φ	Local damage of a particle
λ	Remaining life of the bond
N	Number of wheel load cycles
A, M	Fitting parameters related to the fatigue fracture performance of materials
s, s_0	Bond stretch, critical value of the bond stretch
s^+, s^-	Maximum/minimum values of bond stretch during a single cyclic loading
ε	Bond stretch change under a single cyclic loading
x, y, z	Longitudinal/lateral/vertical direction of the railway line
Δ	Discrete size of particles
ΔK	Range of stress intensity factor
μ	Wheel-rail friction coefficient
q, q_0	Crack length, initial crack length , initial crack angle
β, θ	Initial crack angle, propagation angle of the crack

crystallographic orientation on oblique railhead crack propagation. Liu et al. [13] analysed the effects of martensitic transformation and inclusions on railhead crack propagation through metallographic observations. Benoit et al. [14] analysed the relationship between fatigue cracks and the plastic deformation of pearlitic rails from the perspective of microstructure. Haidemenopoulos et al. [15] performed a metallurgical analysis of in-service railhead material and studied the characteristics of its crack propagation. Larijani et al. [16] studied the effects of the anisotropy of pearlitic rail material on crack propagation.

Experimental studies usually take a long time and require a high budget; thus, analytical and computer-aided simulations are conducted as alternatives. To date, researchers have studied the trends and paths of railhead crack propagation using theories or methods such as fracture mechanics [17,18], the extended finite element method [19,20], the cohesive zone method [2,21] and the boundary element method [22,23]. However, these crack research methods usually require many high-level modelling techniques, such as crack tip remeshment, the use of singular elements, or reinforcement functions, which makes the research too complicated and requires extra effort. Moreover, there remain great challenges in the complex propagation process with respect to the simulation of crack branching, oscillation and merging [24].

To better consider the problem of discontinuous deformation, Silling [25] proposed the framework of peridynamic theory. In peridynamic theory, an integral model is used in place of the classic partial differential model, thus avoiding the invalidation problem, which usually appears under the classic mathematical framework due to discontinuity. After more than twenty years of development, peridynamic theory is now widely used in the study of elastic wave propagation [26], composite material fracture [27], rock failure [28] and corrosion damage [29], etc. Recently, with the advantages of dealing with fracture problems such as crack propagation, peridynamic theory has been preliminarily applied to the analysis of railway fatigue. Freimanis et al. [30] simulated rail squat initiation and growth using the peridynamic theory. In the authors' previous work [31], a two-dimensional bond-based peridynamic model for prediction of fatigue crack initiation in railheads was established and validated. The Poisson's ratio of a material is restricted to a fixed value in the bond-based peridynamics [25,32]. However, in railway engineering, it usually involves various kinds of materials in multi-states whose Poisson's ratio cannot keep consistent with the fixed value. Thus, this will limit the applications of bond-based peridynamics in railway engineering. While for an ordinary state-based model, there is no such limitation. In this work, the ordinary state-based peridynamic theory is employed to investigate the process of fatigue crack propagation at the railhead surface.

This paper is organized as follows. The theory of ordinary state-based peridynamics and the method to analyse fatigue crack propagation are briefly summarized in Section 2. Section 3 introduces the detailed modelling approach and the calculation process. In

Section 4, the proposed model is verified in terms of rail quasi-static deformation and the fatigue failure of rail material. Then, in Section 5, parameter studies are conducted, including the effects of the initial crack angle, initial crack length and wheel-rail friction coefficient on crack propagation. Finally, Section 6 presents the conclusions and future research possibilities.

2. Peridynamic theory for fatigue analysis

2.1. Ordinary state-based peridynamic theory

In peridynamic theory [25], as shown in Fig. 1, the object is discretized as a particle group. There is an interaction between a particle $\mathbf{x}$ and another particle $\mathbf{x}'$ in its horizon H, where $\mathbf{x}' \in H$, $||\mathbf{x}' - \mathbf{x}|| < \delta$, and δ represents the radius of the horizon H. The initial bond vector $\boldsymbol{\xi} = \mathbf{x}' - \mathbf{x}$. When the object is deformed, the respective displacement vectors of the two particles are $\mathbf{u}$ and $\mathbf{u}'$. The relative displacement vector of the two particles is $\boldsymbol{\eta} = \mathbf{u}' - \mathbf{u}$; thus, the bond vector in the current configuration Ω_t of the object becomes $\boldsymbol{\xi} + \boldsymbol{\eta}$.

According to Newton's second law, the equilibrium equation of a particle with the theory of ordinary state-based peridynamics can be written as [33]:

$$\rho\ddot{\mathbf{u}}(\mathbf{x},t) = \int_H \{\underline{\mathbf{T}}[\mathbf{x},t]\langle\boldsymbol{\xi}\rangle - \underline{\mathbf{T}}[\mathbf{x}',t]\langle-\boldsymbol{\xi}\rangle\}dH + \mathbf{b}(\mathbf{x},t) \tag{1}$$

where ρ is the density of the object, $\mathbf{b}$ is the external force density, and $\underline{\mathbf{T}}[\mathbf{x},t]$ and $\underline{\mathbf{T}}[\mathbf{x}',t]$ are the pairwise force vectors that act on $\mathbf{x}$ and $\mathbf{x}'$, respectively.

This paper simplifies the railhead deformation to a plane strain problem [2], and the force vector is [34]:

$$\underline{\mathbf{T}}[\mathbf{x},t]\langle\boldsymbol{\xi}\rangle = \left\{2\frac{\underline{w}\cdot\underline{x}}{q_s}\cdot K\cdot\theta_s + \frac{8G}{q_s}\cdot\underline{w}\cdot\underline{e}_s^d\right\}\frac{\boldsymbol{\xi}+\boldsymbol{\eta}}{\|\boldsymbol{\xi}+\boldsymbol{\eta}\|} \tag{2}$$

in which the influence function and the reference position function are

$$\underline{w} = \delta/\|\boldsymbol{\xi}\| \tag{3}$$

$$\underline{x} = \|\boldsymbol{\xi}\| \tag{4}$$

The bulk modulus and the shear modulus are

$$K = \frac{E}{2(1+v)(1-2v)} \tag{5}$$

$$G = \frac{E}{2(1+v)} \tag{6}$$

where E and v are the Young's modulus and Poisson's ratio, respectively.

Meanwhile, q_s represents the weighted volume, θ_s represents nonlocal plane dilatation, and $\underline{e}_s^d$ represents the plane deviatoric extension scalar state. The formulas for q_s, θ_s and $\underline{e}_s^d$ are as follows.

$$\begin{cases} q_s = (\underline{w}\cdot\underline{x})\bullet\underline{x}\theta_s = 2\cdot(\underline{w}\cdot\underline{x})\bullet(\|\boldsymbol{\xi}+\boldsymbol{\eta}\|-\|\boldsymbol{\xi}\|)/q\underline{e}_s^d = (\|\boldsymbol{\xi}+\boldsymbol{\eta}\|-\|\boldsymbol{\xi}\|)-\theta_s\cdot\underline{x}/2 \end{cases} \tag{7}$$

where the dot product ($\bullet$) of two states and its properties are defined in [33]. The calculation process for $\underline{\mathbf{T}}[\mathbf{x}',t]$ is similar to that of $\underline{\mathbf{T}}[\mathbf{x},t]$ (see references [33;34] for details).
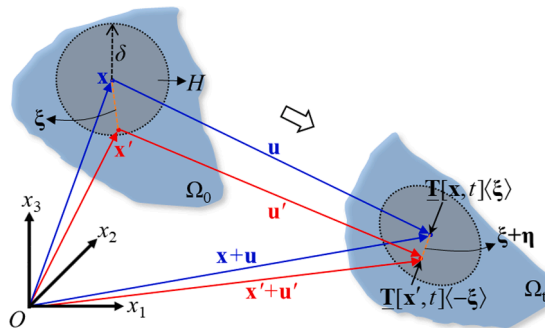

Fig. 1. Schematic diagram of particle interaction during the deformation of an object.

The above formulations of ordinary state-based peridynamic theory are presented at the continuum level. To be applied in practice, these formulations need to be numerically discretized according to the situations of an actual case. For the information of how to numerically discretize these formulations, readers can find more details in [35], where the standard discretization methods of peridynamic models are provided.

2.2. Analysis method for fatigue crack propagation in ductile materials

To consider the damage in the deformation process, a scalar function, ψ, is introduced into the force vector states [36]. The modified particle motion equilibrium equation is as follows.

$$
\begin{cases}
\rho \ddot{\mathbf{u}}(\mathbf{x}, t) = \displaystyle\int_H \psi[\boldsymbol{\xi}, t]\{\underline{\mathbf{T}}[\mathbf{x}, t]\langle \boldsymbol{\xi}\rangle - \underline{\mathbf{T}}[\mathbf{x}', t]\langle -\boldsymbol{\xi}\rangle\}dH + \mathbf{b}(\mathbf{x}, t) \\[2mm]
\psi[\boldsymbol{\xi}, t] = \begin{cases} 1, \text{ if } \boldsymbol{\xi} \text{ is unbroken} \\ 0, \text{ otherwise} \end{cases}
\end{cases}
\tag{8}
$$

When ψ is 0, the bond of the two particles is broken, and their interaction is eliminated.

The local damage φ of a particle is defined as the ratio of the broken bonds to the initial bonds.

$$
\varphi[x, t] = 1 - \frac{\int_H \psi[\boldsymbol{\xi}, t]dH}{\int_H dH}
\tag{9}
$$

Cracks propagate gradually in the railhead under cyclic wheel loading because rail steel is a ductile material. Considering the fatigue fracture behaviour of ductile materials, Silling and Askari proposed a fatigue damage analysis method in peridynamics [37]. The accuracy of this method is further proven in [38]. In this method, each bond has a remaining service life λ running from 1 to 0 (broken). The relationship between λ and the number of load cycles N is given in Equation (10), and this relationship is the fatigue failure model.

$$
\begin{cases}
\dfrac{d\lambda}{dN} = -A \cdot \varepsilon^M \\[2mm]
\varepsilon = |s^+ - s^-| \\[2mm]
s = (\|\boldsymbol{\xi} + \boldsymbol{\eta}\| - \|\boldsymbol{\xi}\|)/\|\boldsymbol{\xi}\|
\end{cases}
\tag{10}
$$

where A and M are constants related to the fatigue fracture performance of the material. These two constants will be further discussed in Section 3.3. s^+ and s^- represent the maximum and minimum values of bond stretching, respectively. ε represents the variation amplitude of bond stretching. If ε exceeds the bond stretch limitation of the rail material, s_0, the bond will directly break. In this paper, s_0 is 0.112 [31].

3. Simulation model of fatigue crack propagation in railhead

As shown in Fig. 2, in the Cartesian coordinate system $oxyz$, x is the train's moving direction (longitudinal direction), y is the lateral direction and z is the vertical direction. In this paper, a two-dimensional peridynamic model is built in the oxz plane to analyse fatigue crack propagation in railheads. The size of the model is $w_1 \times h_1$. According to the suggestions in [39], the mesh size should be as fine as possible and the mesh size close to the cracks should be no coarser than 0.1 mm $\times$ 0.1 mm. To strike a balance between the computational accuracy and efficiency, this paper selects a small crack propagation zone ($w_2 \times h_2$) from the whole model, as shown
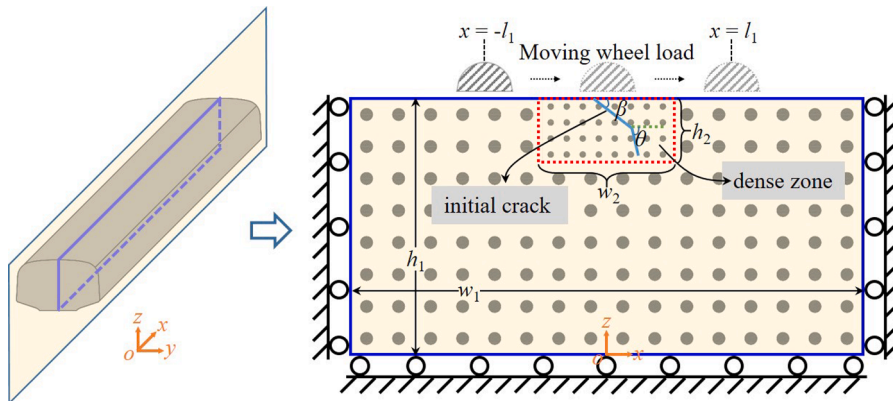

Fig. 2. Two-dimensional peridynamic model for fatigue crack propagation in railheads.

with the red dashed line in Fig. 2. The mesh in this crack propagation zone is fine, with each particle covering 0.1 mm × 0.1 mm, while the other part of the model has a coarse mesh. The radius of the horizon is 3.015 times the mesh size [40].

Uniform discretization is the conventional method used to implement peridynamics. This is very inefficient when a localized area requires a dense particle spacing. The varied particle spacing discretization method can overcome this shortcoming but leads to ghost forces in static cases and spurious wave reflections in dynamic problems. At present, some methods have been proposed to solve the problems caused by the varied particle spacing discretization in peridynamics. Ren et al. [41] developed a dual-horizon peridynamics formulation that naturally includes varying horizon sizes. This method was introduced to consider the unbalanced interactions between the particles with different horizon sizes. Shojaei et al. [32] proposed a method to couple grids with different spacings and developed an efficient algorithm for adaptive refinement. Bazazzadeh et al. [42] built a thermomechanical peridynamic model using adaptive grid refinement, and varied particle spacing discretization was allowed in this model. The method of dual-horizon peridynamics is adopted to treat the varied particle spacing discretization of the model in this work.

The effect of the moving wheel load is considered in this model. The wheel load moves in the range of $[-l_1, l_1]$. As depicted in Fig. 2, at the two lateral boundaries, there is no longitudinal displacement in the x direction. At the bottom boundary, there is no vertical displacement in the z direction [39]. All the bonds passing through the predefined initial crack are broken [43]. β represents the angle of the initial crack, and q_0 represents the length of the initial crack. θ is the propagation angle of the new crack extending from the initial crack.

Table 1 lists the values of the parameters of this model.

3.1. Wheel load

Hertz contact theory is used in the calculation of the wheel-rail contact. As shown in Fig. 3, the spatial distribution of the wheel load is semi-ellipsoidal. Carter's two-dimensional rolling contact theory [44] is employed to calculate the normal wheel-rail contact stress, producing an equivalent two-dimensional rectangular wheel load from the usual elliptical contact patch. As shown in Fig. 3, a and b represent the semi-major axis and semi-minor axis of the elliptical contact patch, respectively. b_0 represents the lateral equivalent width of the contact patch. The tangential force will be further determined considering different friction coefficients.

3.2. Contact of the two surfaces of a crack

In peridynamics, after the long-range interaction between two particles disappears, the particles may overlap with each other in terms of position [25]. This is physically unacceptable. To prevent the crack surfaces from penetrating each other, it is necessary to set the contact of the crack surfaces in the model shown in Fig. 2. When there is no long-range interaction between two particles, a short-range repulsive force can be applied to simulate crack surface contact. The calculation method is as follows [45]:

$$\mathbf{f}_{sh} = \frac{\boldsymbol{\xi} + \boldsymbol{\eta}}{\|\boldsymbol{\xi} + \boldsymbol{\eta}\|} min\left\{0, \frac{120\mu}{\pi b_0 \delta^3}\left[\frac{\|\boldsymbol{\xi} + \boldsymbol{\eta}\|}{\Delta}\right] - 1\right\} \tag{11}$$

where Δ represents the particle mesh size. The effectiveness of this contact calculation method is verified in [43].

3.3. Fatigue failure model of rail steel material

The fatigue failure model of the rail steel material is determined through compact-tension tests [37]. Zhong et al. [46] reported the results of fatigue tension tests on U71Mn rail. The dimensions of the compact tensile specimen are shown in Fig. 4 (defined in ASTM E647-15e1 [47]). The maximum tension of the cyclic load exerted on the specimen is $P_{max} = 10.5$ kN, and the loading coefficient $R = 0.1$.

The variation in the stress intensity factor, ΔK, under cyclic loading can be calculated using the following formula:

$$\Delta K = \frac{P_{max}(1-R)}{B\sqrt{W}}\frac{(2+\alpha)}{(1-\alpha)^{3/2}}(0.886 + 4.64\alpha - 13.32\alpha^2 + 14.72\alpha^3 - 5.6\alpha^4) \tag{12}$$

where $\alpha = q/W$. With the test results in [46], the relationship between the crack propagation rate dq/dN and ΔK could be derived, as shown with the black straight line in Fig. 5. The Paris law is adopted:

$$dq/dN = 1.7861e - 9\Delta K^{3.3595} \tag{13}$$

Thus, $M = 3.3595$ (see Equation (10)). Assuming $A = A_{trial} = 1000$, and following the method and procedures in [48], a peridynamic model is built to simulate the compact-tension tests. The simulation results are shown in Fig. 6.

With the simulation results in Fig. 6, the fitting curve with Paris law for the peridynamic analysis is updated as follows.

Table 1
Parameters of the peridynamics model.

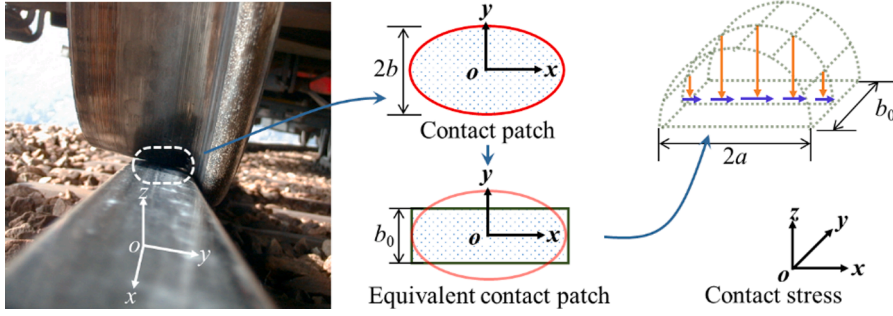| E	ν	w_1	h_1	w_2	h_2	l_1
205 GPa	0.3	80 mm	40 mm	20 mm	5.2 mm	20 mm

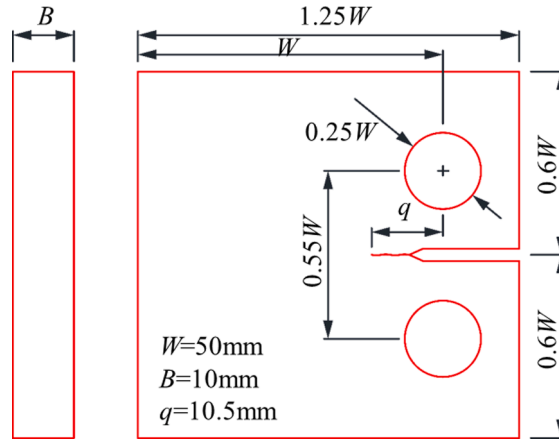**Fig. 3.** Wheel load on the railhead.

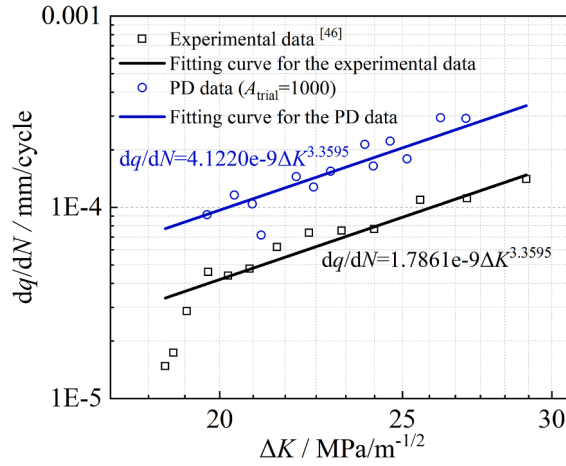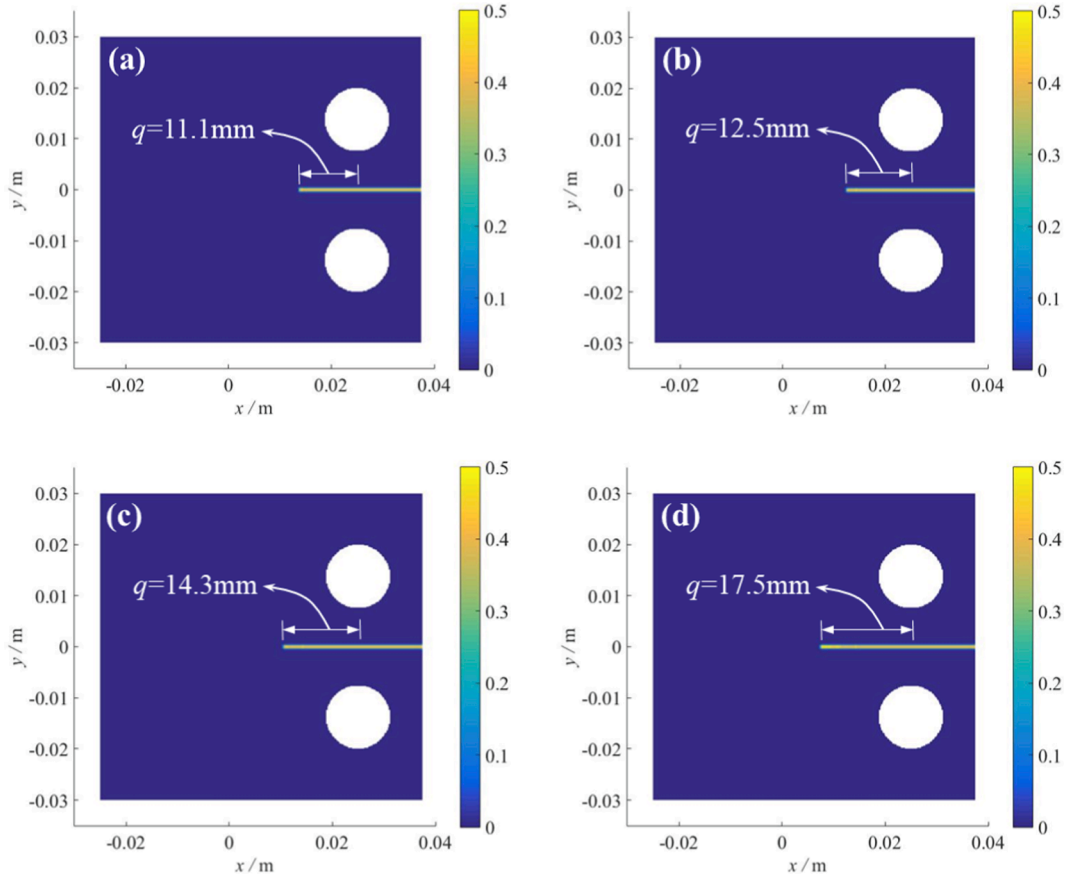**Fig. 4.** Dimensions of a compact-tension specimen.

Fig. 5. Fatigue crack propagation rate curve.

$$\mathrm{d}q/\mathrm{d}N = 4.1220e - 9\Delta K^{3.3595} \tag{14}$$

According to Equations (13) and (14), the value of A can be updated as [37]:

$$A = A_{\mathrm{trial}} \times \frac{1.7861 \times 10^{-9} \Delta K^{3.3595}}{4.1220 \times 10^{-9} \Delta K^{3.3595}} = 1000 \times \frac{1.7861 \times 10^{-9}}{4.1220 \times 10^{-9}} = 433.31 \tag{15}$$

Fig. 6. Simulation results of crack propagation (colour bar is local damage φ). (a) 12,796 cycles; (b) 26,185 cycles; (c) 40,228 cycles; (d) 54,010 cycles.

3.4. Numerical calculation method and process

To conduct the calculation of fatigue crack propagation, a program is established using the Fortran language. The calculation flow is as follows.

Step 1: Input the parameters and apply model boundary conditions.

Step 2: Use an adaptive dynamic relaxation (ADR) method [49] to perform a quasi-static analysis of the wheel load in a one-way process from $x = -l_1$ to $x = l_1$.

Step 3: Directly break the corresponding bond if the amplitude ε of bond stretch is greater than the limiting value s_0. Otherwise, break the bond according to the maximum ε, and use Equation (6) to determine how many cycles it needs to break the bond. Add the number of load cycles to the total load cycles.

Step 4: Update the remaining fatigue life of each bond and break the corresponding bond if the remaining fatigue life is reduced to 0.

Step 5: If the number of total load cycles reaches the set value, end the calculation and output the results; if it does not reach the set value, then go to step 1 for a new calculation.

4. Model verification

In this section, the proposed model is verified in terms of two aspects. One is the rail deformation under the quasi-static load, and the other is the fatigue failure model of the rail steel material.

4.1. Rail deformation under the quasi-static load

To verify (without considering fatigue), a finite element (FE) model is built. This FE model has the same mesh and boundary conditions as that of the proposed peridynamic model. The rail steel material is linearly elastic with a Young's modulus of 2.1E5 MPa

and Poisson's ratio of 0.3. The wheel-rail friction coefficient is 0.3. The wheel normal load is 60.8 kN (thus, the tangential load is 18.2 kN. For the contact patch, a is 7.9 mm, b_0 is 6.6 mm). The effect of the moving load is considered in this FE model.

When the load moves to $x = 0$, as shown in Fig. 7, the two models show very similar rail deformation patterns. The results with the peridynamics model have not been averaged; thus, pixelation appears in the displacement diagram. The calculation error of the peridynamic model with respect to the FE model is calculated in terms of displacement within the fine mesh zone at the rail surface, as shown in Fig. 7 (c).

As shown in Fig. 7 (c), based on the FE model, the calculation error of the peridynamic model in the fine mesh zone remains within 12%. Specifically, at the main part [-5 mm, 5 mm] close to the load, the calculation error is much lower, within 3%. Therefore, the proposed peridynamic model can get quite similar results with that of a finite element model in terms of rail deformation under the quasi-static load.

4.2. Fatigue failure model of the rail steel material

The compact-tension tests are simulated again using the proposed peridynamic model with the updated material model constants ($A = 433.31$, $M = 3.3595$). The maximum tension of the cyclic load exerted on the specimen is $P_{max} = 11.5$ kN and the loading coefficient $R = 0.1$. The simulation results are shown in Fig. 8.

Fig. 9 shows a comparison between the simulation results and the test results in [46]. The simulation results are essentially consistent with the test results, verifying the accuracy of the fatigue failure model of the rail material applied in the proposed peridynamic model.
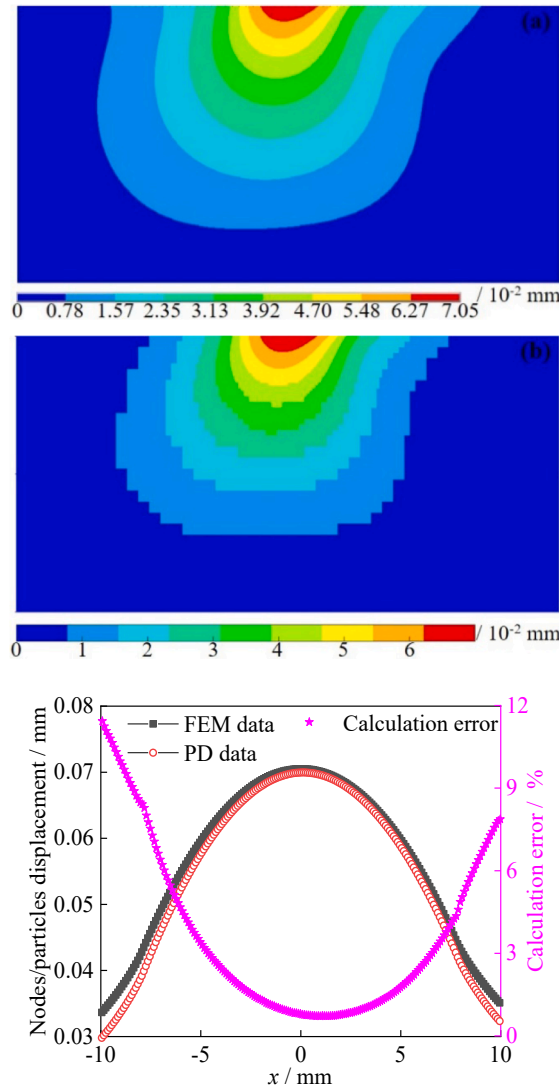

Fig. 7. Calculation results of quasi-static deformation of rail. (a) FE model; (b) peridynamic model; (c) calculation error.

5. Discussion

5.1. Effect of the initial crack angle

An initial crack with a length of 2 mm is arranged at the rail surface, and the wheel-rail friction coefficient is 0.3. The other parameters are the same as those in Section 4.1. Considering 3 cases with initial crack angles of 30°, 45° and 60°, the simulation results with the proposed peridynamic model are shown in Fig. 10.

As shown in Fig. 10, the new cracks are quite similar in shape and length for the 3 cases. All the new cracks have not propagated along the direction of the initial cracks but much more downwards [50]. In addition, the propagation angle of the new cracks gradually decreases during the propagation process [51]. This is probably because of the larger resistance the new cracks come across when they deepen.

The length of the new crack with increasing cycling load in each case is calculated and shown in Fig. 11.

As shown in Fig. 11, the crack propagation rates in the 3 cases gradually increase with increasing cycling loads. The crack propagation rate increases as the initial crack angle varies from 30° to 60°, and a similar finding can be found in [50].

5.2. Effect of the initial crack length

The effect of the length of the initial oblique crack with an angle of 45° is also investigated. The wheel-rail friction coefficient is 0.3. The other parameters are the same as those in Section 4.1. The investigated lengths of the initial oblique cracks are 1.5 mm, 2 mm and 2.5 mm. The simulation results are shown in Fig. 12.

As shown in Fig. 12, the crack propagation paths corresponding to different initial crack lengths are similar. This indicates that the initial crack length varying from 1.5 to 2.5 mm has a very limited effect on the crack propagation paths.

Fig. 13 shows the changes in the length of the new crack with increasing cycling loads given different initial crack lengths.

As shown in Fig. 13, the crack propagation rate increases with increasing initial crack length. With a longer initial crack, the new crack propagates faster. Similar findings can be found in [52].
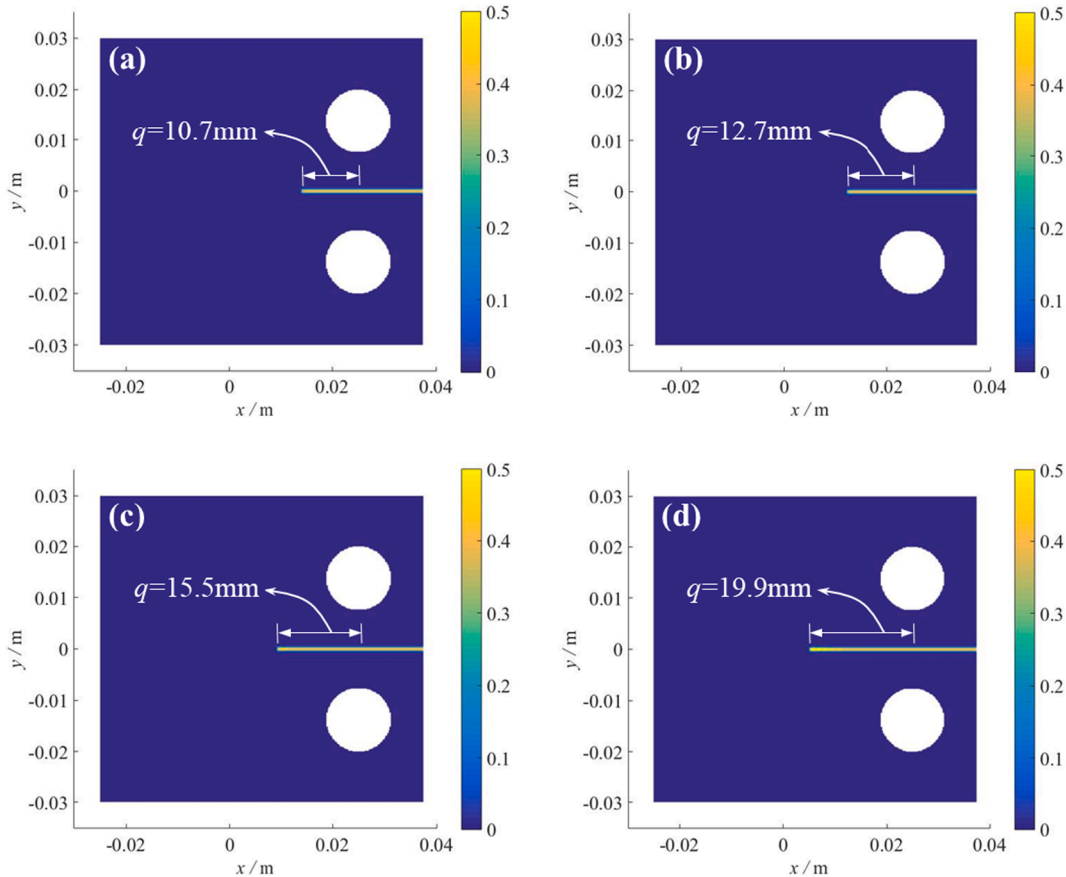
Fig. 8. Peridynamics simulation of crack propagation (colour bar is local damage φ). (a) 12,604 cycles; (b) 47,768 cycles; (c) 79,708 cycles; (d) 103,800 cycles.
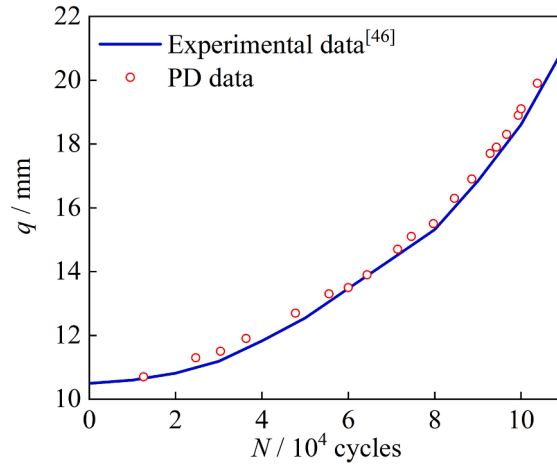
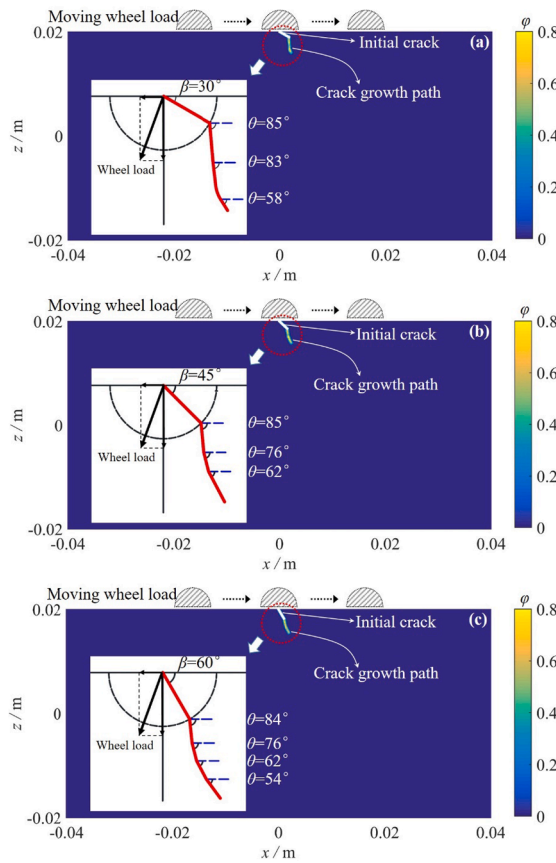**Fig. 9.** Comparison of experimental fatigue life and peridynamic numerical results.

Fig. 10. Simulation results of crack propagation considering different initial crack angles. (a) $\beta = 30°$, after 8,426,100 cycles; (b) $\beta = 45°$, after 7,991,000 cycles; (c) $\beta = 60°$, after 7,445,600 cycles.

5.3. Effect of the wheel-rail friction coefficient

Considering an initial oblique crack with an angle of 45° and length of 1.5 mm, the effect of the wheel-rail friction coefficient is investigated. The 3 cases with different wheel-rail friction coefficients are 0.1, 0.3 and 0.5. The simulation results are shown in Fig. 14, where μ represents the wheel-rail friction coefficient.

As shown in Fig. 14, with different wheel-rail friction coefficients, the new crack varies significantly. The larger the friction
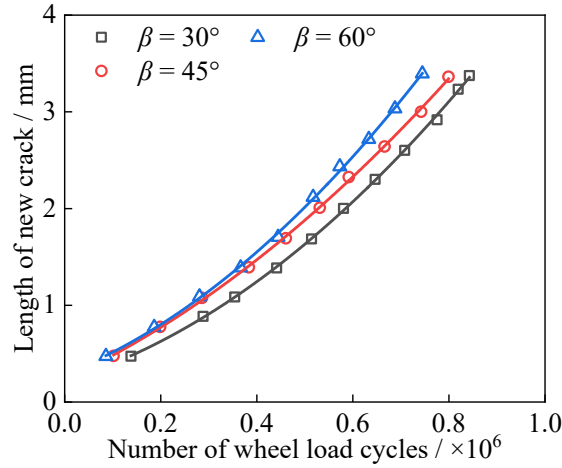
Fig. 11. Length of new crack with the wheel load cycles given different initial crack angles.
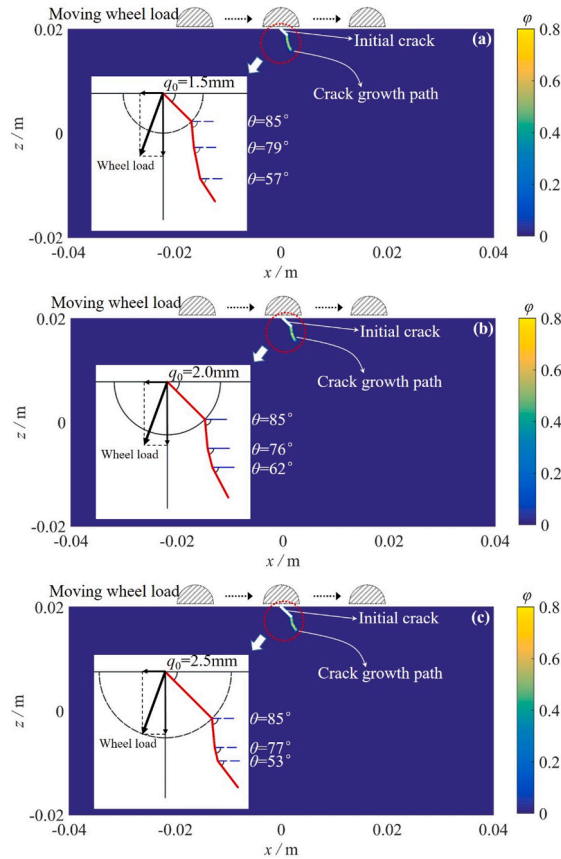

Fig. 12. Simulation results of crack growth given different initial crack lengths. (a) $q_0 = 1.5$ mm, after 9,380,400 cycles; (b) $q_0 = 2$ mm, after 7,991,000 cycles; (c) $q_0 = 2.5$ mm, after 6,677,900 cycles.

coefficient is, the more likely the new crack is to develop downwards. This is probably because the larger friction coefficient produces a larger tangential wheel load (with a constant normal wheel load). This larger tangential wheel load combined with the constant normal wheel load makes the total wheel load larger and more backwards.

Fig. 15 shows the changes in the length of the new crack with increasing cycling loads given different wheel-rail friction coefficients.

As shown in Fig. 15, the wheel-rail friction coefficient has a significant influence on the crack propagation rate. The larger the
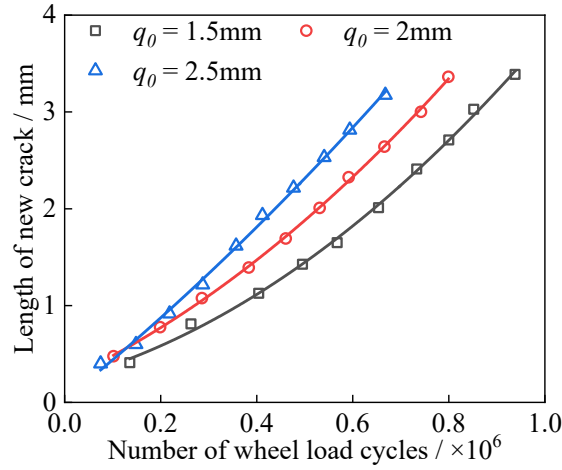
Fig. 13. Length of new crack with the wheel load cycles given different initial crack lengths.
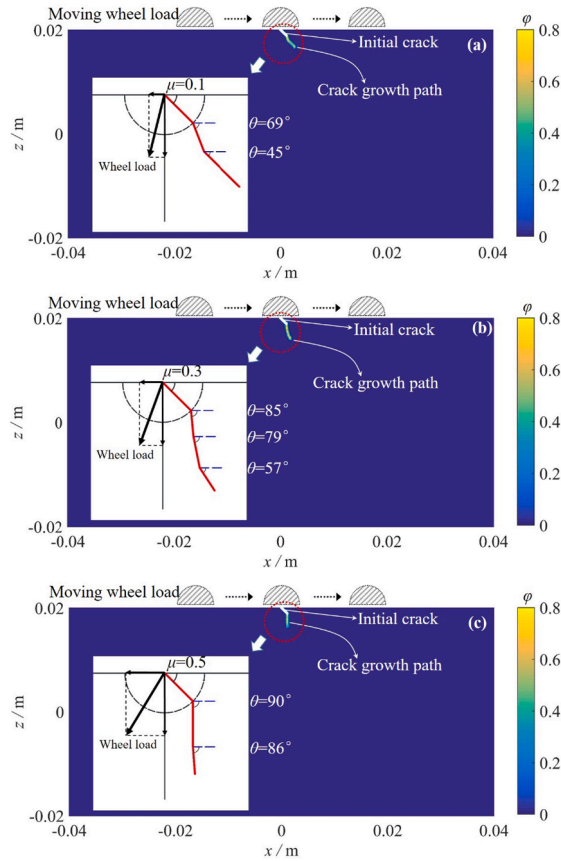

Fig. 14. Simulation results of crack propagation at different wheel-rail friction coefficients. (a) $\mu = 0.1$, after 34,335,000 cycles; (b) $\mu = 0.3$, after 9,380,400 cycles; (c) $\mu = 0.5$, after 2,795,100 cycles.

friction coefficient is, the faster the crack develops. Similar findings can be found in [53].

This finding indicates that proper lubrication measures that make a lower wheel-rail friction coefficient may be able to slow down the crack propagation at the rail surface, thus elongating the rail fatigue life. However, it is worth mentioning that another situation could occur when the lubricant flows into the crack space.
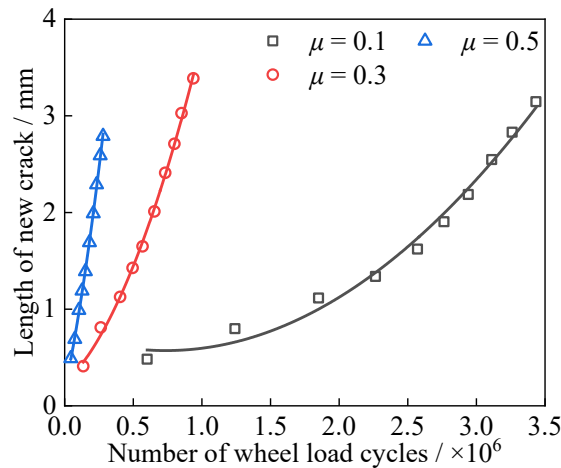
Fig. 15. Length of new crack with the wheel load cycles given different wheel-rail friction coefficients.

6. Conclusions

Based on ordinary state-based peridynamic theory, a 2D peridynamic model was established to investigate surface fatigue crack propagation in railhead. The analysis method for ductile material-related fatigue crack propagation is employed in this model. The proposed model is verified in terms of rail deformation under quasi-static loading and the fatigue failure model of the rail steel material. Good agreements have been achieved not only in comparison with the finite element model in terms of rail deformation but also in comparison with the experimental results in terms of material failure. Then, the proposed model is used to perform parameter analysis. The effects of the initial crack angle, initial crack length and wheel-rail friction coefficient on crack propagation at the railhead surface are studied.

According to the simulation results and discussion presented in Section 5, it is found that with a larger initial crack angle and longer initial crack length, the crack propagation will be faster. The larger the wheel-rail friction coefficient is, the faster the crack develops. Properly reducing the wheel-rail friction coefficient may be a good way to elongate the rail fatigue life. In general, wheel load is the primary factor influencing the direction and speed of crack propagation.

In the future, a three-dimensional peridynamic model will be built; thus, the special wheel-rail contact forces could be considered, which will make the simulations of fatigue crack propagation more realistic. Also, the fatigue failure model of the rail steel material will be updated to make it more suitable for the multifold deformation modes of cracks, such as opening, sliding and tearing.

CRediT authorship contribution statement

Xiaochuan Ma: Conceptualization, Methodology, Writing – original draft. **Li Wang:** Writing – review & editing, Methodology. **Jinhui Xu:** Data curation, Formal analysis. **Qingsong Feng:** Methodology, Investigation. **Linya Liu:** Methodology, Writing – review & editing. **Huapeng Chen:** Methodology, Conceptualization.

Declaration of Competing Interest

The authors declare that they have no known competing financial interests or personal relationships that could have appeared to influence the work reported in this paper.

References

[1] El-sayed HM, Lotfy M, El-din Zohny HN, Riad HS. Prediction of fatigue crack initiation life in railheads using finite element analysis. Ain Shams Eng J 2018;9(4): 2329–42.
[2] Ghodrati M, Ahmadian M, Mirzaeifar R. Modeling of rolling contact fatigue in rails at the microstructural level. Wear 2018;406-407:205–17.
[3] Steenbergen M. Rolling contact fatigue: Spalling versus transverse fracture of rails. Wear 2017;380-381:96–105.

[4] Li Q, Huang X, Huang W. Fatigue property and microstructure deformation behavior of multiphase microstructure in a medium-carbon bainite steel under rolling contact condition. Int J Fatigue 2019;125:381–93.

[5] Zhou L, Wang WJ, Hu Y, Marconi S, Meli E, Ding HH, et al. Study on the wear and damage behaviors of hypereutectoid rail steel in low temperature environment. Wear 2020;456-457:203365. https://doi.org/10.1016/j.wear.2020.203365.

[6] Hardwick C, Lewis R, Stock R. The effects of friction management materials on rail with pre existing rcf surface damage. Wear 2017;384-385:50–60.

[7] Zhao XJ, Guo J, Liu QY, Butini E, Marini L, Meli E, et al. Effect of spherical dents on microstructure evolution and rolling contact fatigue of wheel/rail materials. Tribol Int 2018;127:520–32.

[8] Liu CP, Zhao XJ, Liu PT, Pan JZ, Ren RM. Influence of Contact Stress on Surface Microstructure and Wear Property of D2/U71Mn Wheel-Rail Material. Materials 2019;12(19):3268.

[9] Wang WJ, Lewis SR, Lewis R, Beagles A, He CG, Liu QY. The role of slip ratio in rolling contact fatigue of rail materials under wet conditions. Wear 2017;376-377:1892–900.

[10] Ding HH, Fu ZK, Wang WJ, Guo J, Liu QY, Zhu MH. Investigation on the effect of rotational speed on rolling wear and damage behaviors of wheel/rail materials. Wear 2015;330-331:563–70.

[11] Dhar S, Danielsen HK, Fæster S, Rasmussen C, Zhang Y, Jensen DJ. Crack formation within a Hadfield manganese steel crossing nose. Wear 2019;438-439: 203049. https://doi.org/10.1016/j.wear.2019.203049.

[12] Masoumi M, Sinatora A, Goldenstein H. Role of microstructure and crystallographic orientation in fatigue crack failure analysis of a heavy haul railway rail. Eng Fail Anal 2019;96:320–9.

[13] Liu JP, Zhou QY, Zhang YH, Liu FS, Tian CH, Li C, et al. The formation of martensite during the propagation of fatigue cracks in pearlitic rail steel. Mat Sce Eng A-Struct 2019;747:199–205.

[14] Benoît D, Salima B, Marion R. Multiscale characterization of head check initiation on rails under rolling contact fatigue: Mechanical and microstructure analysis. Wear 2016;366-367:383–91.

[15] Haidemenopoulos GN, Sarafoglou PI, Christopoulos P, Zervaki AD. Rolling contact fatigue cracking in rails subjected to in-service loading. Fatigue Fract Eng M 2016;39(9):1161–72.

[16] Larijani N, Brouzoulis J, Schilke M, Ekh M. The effect of anisotropy on crack propagation in pearlitic rail steel. Wear 2014;314(1-2):57–68.

[17] Andersson R, Kabo E, Ekberg A. Numerical assessment of the loading of rolling contact fatigue cracks close to rail surface irregularities. Fatigue Fract Eng M 2020;43(5):947–54.

[18] Zhao X, Zhao X, Liu C, Wen Z, Jin X. A study on dynamic stress intensity factors of rail cracks at high speeds by a 3D explicit finite element model of rolling contact. Wear 2016;366-367:60–70.

[19] Mai SH, Gravouil A, Nguyen-Tajan ML, Trollé B. Numerical simulation of rolling contact fatigue crack growth in rails with the rail bending and the frictional contact. Eng Fract Mech 2017;174:196–206.

[20] Ranjha SA, Mutton P, Kapoor A. Effect of head wear and lateral forces on underhead radius crack propagation. P I Mech Eng F-J Rai 2014;228(6):620–30.

[21] Ghodrati M, Ahmadian M, Mirzaeifar R. Three-dimensional study of rolling contact fatigue using crystal plasticity and cohesive zone method. Int J Fatigue 2019; 128:105208. https://doi.org/10.1016/j.ijfatigue.2019.105208.

[22] Masoudi Nejad R. Numerical study on rolling contact fatigue in rail steel under the influence of periodic overload. Eng Fail Anal 2020;115:104624. https://doi.org/10.1016/j.engfailanal.2020.104624.

[23] Masoudi Nejad R, Liu Z, Ma W, Berto F. Reliability analysis of fatigue crack growth for rail steel under variable amplitude service loading conditions and wear. Int J Fatigue 2021;152:106450. https://doi.org/10.1016/j.ijfatigue.2021.106450.

[24] Sedmak A. Computational fracture mechanics: An overview from early efforts to recent achievements. Fatigue Fract Eng M 2018;41(12):2438–74.

[25] Silling SA. Reformulation of elasticity theory for discontinuities and long-range forces. J Mech Phys Solids 2000;48(1):175–209.

[26] Ma X, Feng Q, Liu L, Xu J, Zhang P, Chen H. A non-local method in peridynamic theory for simulating elastic wave propagation in solids. Appl Math Model 2022; 103:360–75.

[27] Zhou Wu, Liu D, Liu N. Analyzing dynamic fracture process in fiber-reinforced composite materials with a peridynamic model. Eng Fract Mech 2017;178:60–76.

[28] Ai D, Zhao Y, Wang Q, Li C. Experimental and numerical investigation of crack propagation and dynamic properties of rock in SHPB indirect tension test. Int J Impact Eng 2019;126:135–46.

[29] Jafarzadeh S, Chen Z, Zhao J, Bobaru F. Pitting, lacy covers, and pit merger in stainless steel: 3D peridynamic models. Corros Sci 2019;150:17–31.

[30] Freimanis A, Kaewunruen S. Peridynamic analysis of rail squats. Appl Sci-Basel 2018;8(11):1–18.

[31] Ma X, Xu J, Liu L, Wang P, Feng Q, Xu J. A 2D peridynamic model for fatigue crack initiation of railheads. Int J Fatigue 2020;135:105536. https://doi.org/10.1016/j.ijfatigue.2020.105536.

[32] Shojaei A, Mossaiby F, Zaccariotto M, Galvanetto U. An adaptive multi-grid peridynamic method for dynamic fracture analysis. Int J Mech Sci 2018;144:600–17.

[33] Silling SA, Epton M, Weckner O, Xu J, Askari E. Peridynamic States and Constitutive Modeling. J Elasticity 2007;88(2):151–84.

[34] Zhang H, Qiao P. A two-dimensional ordinary state-based peridynamic model for elastic and fracture analysis. Eng Fract Mech 2020;232:107040. https://doi.org/10.1016/j.engfracmech.2020.107040.

[35] Shojaei A, Hermann A, Cyron CJ, Seleson P, Silling SA. A hybrid meshfree discretization to improve the numerical performance of peridynamic models. Comput Methods Appl Mech Engrg 2022;391:114544. https://doi.org/10.1016/j.cma.2021.114544.

[36] Silling SA, Bobaru F. Peridynamic modeling of membranes and fibers. Int J Nonlin Mech 2005;40(2-3):395–409.

[37] Silling SA, Askari A. Peridynamic model for fatigue cracking Tech. rep. no. SAND2014-18590. Albuquerque (NM, United States): Sandia National Laboratories (SNL-NM) 2014.

[38] Zhang G, Le Q, Loghin A, Subramaniyan A, Bobaru F. Validation of a peridynamic model for fatigue cracking. Eng Fract Mech 2016;162:76–94.

[39] Kráčalík M, Daves W, Antretter T. Calculation of crack driving forces of surface cracks subjected to rolling/sliding contact. Eng Fract Mech 2016;152:10–25.

[40] Silling SA, Askari A. A meshfree method based on the peridynamic model of solid mechanics. Comput Struct 2005;83(6):1526–35.

[41] Ren H, Zhuang X, Cai Y, Rabczuk T. Dual-horizon peridynamics. Int J Numer Meth Eng 2016;108(12):1451–76.

[42] Bazazzadeh S, Mossaiby F, Shojaei A. An adaptive thermo-mechanical peridynamic model for fracture analysis in ceramics. Eng Fract Mech 2020;223:106708. https://doi.org/10.1016/j.engfracmech.2019.106708.

[43] Madenci E, Oterkus E, editors. Peridynamic Theory and Its Applications. New York, NY: Springer New York; 2014.

[44] Carter FW. On the action of locomotive driving wheel. Proceeding of Royal Society of London 1926:151–7.

[45] Silling SA. EMU user's manual, Code Ver. 2.6d. Albuquerque (NM, United States): Sandia National Laboratories (SNL-NM) 2004.

[46] Zhong W, Hu JJ, Li ZB, Liu QY, Zhou ZR. A study of rolling contact fatigue crack growth in U75V and U71Mn rails. Wear 2011;271(1-2):388–92.

[47] ASTM E647-15e1, Standard Test Method for Measurement of Fatigue Crack Growth Rates. ASTM International West Conshohocken, PA, 2015, www.astm.org.

[48] Nguyen CT, Oterkus S, Oterkus E. An energy-based peridynamic model for fatigue cracking. Engng Fract Mech 2021;241:107373. https://doi.org/10.1016/j.engfracmech.2020.107373.

[49] Kilic B, Madenci E. An adaptive dynamic relaxation method for quasi-static simulations using the peridynamic theory. Theor Appl Fract Mec 2010;53(3): 194–204.

[50] Trollé B, Baietto M-C, Gravouil A, Mai SH, Prabel B. 2D fatigue crack propagation in rails taking into account actual plastic stresses. Eng Fract Mech 2014;123: 163–81.

[51] Al-Juboori A, Zhu H, Wexler D, Li H, Lu C, McCusker A, et al. Evolution of rail surface degradation in the tunnel: The role of water on squat growth under service conditions. Eng Fract Mech 2019;209:32–47.

[52] Masoudi Nejad R, Shariati M, Farhangdoost K. Effect of wear on rolling contact fatigue crack growth in rails. Tribol Int. 2016;94:118–25.

[53] Seo J-W, Kwon S-J, Lee D-H, Choi H-Y. Analysis of contact fatigue crack growth using twin-disc tests and numerical evaluations. Int J Fatigue 2013;55:54–63.